Journal of Applied Physics

RESEARCH ARTICLE | JUNE 13 2025

The strong spectral- and time-dependent emission of NV center charge state in bulk diamonds

Ashish Redhu ; Rahul Dhankhar ; Sushmita Dey; Rajesh V. Nair

J. Appl. Phys. 137, 223107 (2025)
https://doi.org/10.1063/5.0272720

Journal of Applied Physics ARTICLE pubs.aip.org/aip/jap

The strong spectral- and time-dependent emission of NV center charge state in bulk diamonds

Cite as: J. Appl. Phys. **137**, 223107 (2025); doi: 10.1063/5.0272720
Submitted: 26 March 2025 · Accepted: 27 May 2025 ·
Published Online: 13 June 2025

Ashish Redhu,[1] Rahul Dhankhar,[1] Sushmita Dey,[2] and Rajesh V. Nair[1,a)]

AFFILIATIONS

[1]Laboratory for Nano-Scale Optics and Meta-Materials (LaNOM), Department of Physics, Indian Institute of Technology Ropar, Rupnagar, Punjab 140001, India
[2]Gleam Innovations Pvt. Ltd., Bangalore, Karnataka 560024, India

[a)]**Author to whom correspondence should be addressed:** rvnair@iitrpr.ac.in

ABSTRACT

We discuss charge state ratio-dependent spectral and temporal emission properties of nitrogen-vacancy (NV) centers in bulk diamonds. An understanding of the charge state ratio in artificially grown diamonds is important to design them for NV-based magnetometry. We show that the NV charge state ratio strongly correlates with the intensity of the zero-phonon line (ZPL) of NV^-, which is supported by an emission dip at 2.87 GHz in spin-selective optical transitions. The Debye–Waller factor of NV centers depends on the charge state ratio, and it increases for NV^- with an increase in the charge state ratio. We observe that the energy separation between the second phonon sideband (PSB) and ZPL does not scale multiplicatively with that of the energy separation between first PSB and ZPL. This deviation becomes more pronounced with an increase in charge state ratio, suggesting anharmonicity of vibrational energy levels, rather than the usually reported harmonicity. Further, we discuss the inherent relation between decay rates and charge states as a function of emission wavelengths. The excited state lifetime of NV^0 remains constant, whereas the NV^- lifetime decreases with an increase in the charge state ratio, with an overall decrease of 37%. Our results show an emission spectra-based approach to estimate the charge state ratio in diamond crystals, which is helpful for quantum-enhanced sensing and magnetometry.

I. INTRODUCTION

The nitrogen-vacancy (NV) centers in diamonds are extensively studied defects due to their exceptional properties, such as the ability to undergo spin-selective optical transitions and long coherence times.[1–3] These properties are essential for coherent manipulation and optical readout of spin states, making NV centers highly suitable for memory devices and registers.[4] It has been shown that the NV center is useful for producing stable single photons at room temperature, nanoscale thermometry, and optical metrology.[5,6] Their recent commercialization has leveraged NVs coupled to atomic force microscopy (AFM) tips, facilitating nanoscale probing of magnetic fields with high sensitivity and resolution.[7] The NV center exists in two charge states: neutral nitrogen-vacancy (NV^0) and negatively charged nitrogen-vacancy (NV^-). The spin and optical properties exhibited by the NV^- center make it the desired charge state and establish it as the focus of extensive studies.[8,9] However, both charge states coexist, and the exclusive attainment of NV^- is challenging due to factors, such as growth conditions, thermodynamic equilibrium, annealing, irradiation, and localized charge dynamics.[10] Recently, studies have stressed upon achieving a high NV^-/NV^0 charge state ratio, focusing on the stability of NV^- charge state with a low concentration of NV^0. This high charge ratio can be increased by neutron irradiation,[11] electrical and optical manipulations,[12] surface termination with *n*-type dopant,[13,14] and oxygenated annealing.[15] The interplay between two charge states can interfere with spin dynamics and, therefore, may limit the applicability of NV center in quantum sensing.[8,16] However, there has been a limited study on charge state ratio-dependent emission properties of NV centers.

Here, we discuss charge state ratio-dependent emission intensity and lifetime of NV center in chemical vapor deposition grown diamond samples using extensive photoluminescence (PL) measurements, supported by optically detected magnetic resonance

(ODMR) measurements. Since both charge states can be differentiated by their PL spectra, we have explored the spectroscopic properties, focusing on zero-phonon line (ZPL) and phonon sidebands (PSBs) wavelengths and linewidths, which are used to determine the charge state ratio. The charge state ratio estimated using PL measurements is substantiated by ODMR measurements with better ODMR dip observed for samples with a high charge state ratio. An improved NV^- ZPL and reduced NV^- lifetime is observed with an increased charge state ratio at room temperature. The local environment, particularly the refractive index of NV center surroundings and electromagnetic environments, influences the excited state lifetime. While studies have explored the impact of different-sized nanodiamonds and different excitation wavelengths on excited state lifetime, a spectral-dependent and charge state-dependent lifetime of NV center has yet to be explored. The multiple charge states of NVs are studied using time-resolved emission spectroscopy, revealing a maximum of 37% decrease in lifetime with an increase in emission wavelength and charge state ratio. The PL emission measurements combined with ODMR measurements complement the presence of charge states in diamond samples. These results contribute to the broader understanding of the photo-physics of NV centers, highlighting the importance of the charge state ratio in determining the emission properties and excited state lifetime.

II. MATERIALS AND METHODS

We use seven distinct synthetic diamond samples (M/S. Gleam Innovations Pvt. Ltd., India), and each sample is labeled as SD1 through SD7. The samples are grown in a 6 kW microwave plasma chemical vapor deposition reactor using a mixture of methane, hydrogen, and nitrogen gas with a controlled flow rate. The nitrogen flow rate varied between samples at different values during the growth process, resulting in samples with different nitrogen concentrations. The diamond defects are created using ion irradiations of varying doses, which gives them colors. All samples were exposed to hydrogen plasma etching for half an hour before deposition to eliminate the possibility of any surface defects. The Raman spectra are measured using 50× objective (Olympus) of numerical aperture (NA) 0.50 with identical acquisition parameters (LabRAM HR Evolution; HORIBA). The emission intensity and decay rates are measured using a home-built confocal emission setup in the reflection geometry. We use a 532 nm dual-mode laser (LDH-D-FA-530L; PicoQuant) to excite the samples. The samples are excited, and the emission is collected through the same 60× objective (Nikon) with an NA of 0.95. The emitted light is filtered using a 532 nm dichroic filter and sent to the spectrometer (Kymera328i; ANDOR) equipped with an EMCCD camera (CCD-27332; Newton) for spectral measurements. The PL spectra for the first six samples are acquired at an excitation power of 6.7 μW measured at the entrance of the focusing objective, except for the SD7 sample. At low-power excitation, the SD7 sample shows low emission intensity. Thus, a higher excitation power of 300 μW is employed to enhance the signal-to-noise ratio and facilitate clear identification of PL features for the SD7 sample. Subsequently, the spectra obtained from the SD7 sample are normalized to match the 6.7 μW excitation power. The PL spectroscopy is used to estimate the nitrogen concentration in the samples.

For time-resolved emission measurements, we operate a 532 nm laser in pulsed mode (pulse width: <100 ps, repetition rate: 5 MHz). We pass the collected emission through bandpass filters and, finally, it is collected by a single photon detector (SPCM-AQRH-46-FC, Excelitas Technologies). A time correlator (HydraHarp 400; PicoQuant) is synchronized with detector and laser, creating a histogram of time corresponding to differences between excitation and photon detection events. We use a flip mirror to direct emission to a spectrometer or a single photon detector, thus enabling PL and time-resolved PL measurements from the same location on the sample. Optically detected magnetic resonance (ODMR) is a technique that integrates optical emission measurement with electron spin resonance spectroscopy. To generate an ODMR signal from diamond samples, the 532 nm laser was continually applied, and an analog signal generator (N5181B; Keysight) swept the microwave frequency, and the corresponding changes in PL emission intensity were measured.

III. RESULTS AND DISCUSSIONS

Figure 1(a) shows the measured Raman spectra corresponding to all seven samples using 785 nm laser excitation. We observe the Raman peak at 1332 cm^{-1}; the signature of the diamond structure corresponds to first-order triply degenerated T_{2g} optical phonon excitation at the Brillouin zone center.[17] The 785 nm is outside the absorption band of both charge states of NV and, hence, the sole contribution in this case arises from Raman scattering. Samples SD1, SD2, SD3, SD4, and SD5 show flat backgrounds, while the SD6 and SD7 samples show slopy backgrounds with broad features around 1170–1450 cm^{-1}, which arise due to non-diamond carbon (sp^2) present in the sample.[18–22] However, these features are absent under 473 and 532 nm excitation (Fig. S1 in the supplementary material). It has been shown that a small amount of non-diamond carbon can be detected most sensitively using low-energy excitation (near-IR excitation) in bulk samples. However, the Raman diamond peak is efficiently resolved with high-energy excitation for nanocrystalline diamonds. Hence, the observation of the Raman diamond peak even at 785 nm excitation shows the long-range periodicity of the diamond samples. The position and intensity of the Raman band originating from non-diamond carbon show a variation due to different resonance conditions of sp^2 and sp^3 carbon atoms.[23,24] A small amount of non-diamond carbon features, which are not visible under high-energy excitation, becomes visible upon lower-energy excitation. At the same time, diamond Raman peak intensity decreases; however, there has been limited study focused on understanding the origin of these peaks.[23] Thus, the analysis of Raman spectra confirms that SD2 to SD5 samples are better in terms of long-range lattice crystallinity. Furthermore, SD6 and SD7 samples contain non-diamond carbon impurities, which are due to amorphous carbon at grain boundaries.

Raman mapping is employed to visualize the spatial distribution of peak position, height, or intensity, contingent on the specific application. We have collected a comprehensive set of 400 spectra for confocal Raman mapping, obtained from an array covering 20 × 20 locations across the diamond surface. Each location on the sample surface is spatially separated from its adjacent counterpart by a distance of 1 μm. Subsequently, these spectra are

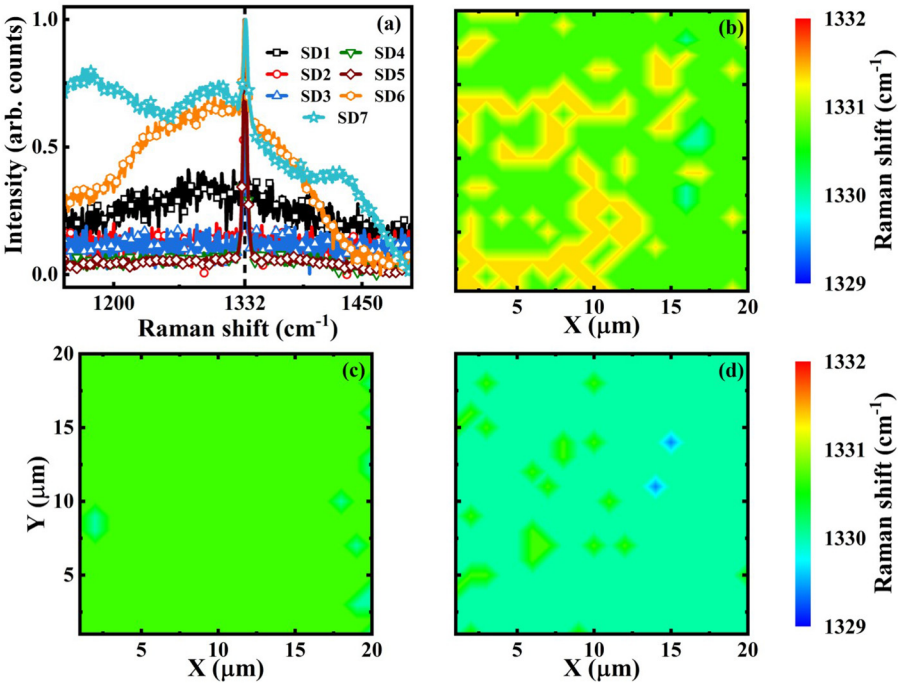

FIG. 1. (a) Raman spectra of diamond samples under 785 nm laser excitation. The sharp Raman shift at 1332 cm^{-1} is the diamond Raman line. Under 785 nm excitation, all samples showed diamond Raman shift; SD6 and SD7 also showed broadband features arising from non-diamond carbon. Raman confocal mapping of (b) SD1, (c) SD4, and (d) SD6 samples under 785 nm laser excitation. The Raman mapping shows a uniform diamond Raman shift across the SD4 diamond surface.

stitched to generate the image encapsulating the entire surface morphology of the diamond sample. Figures 1(b)–(1d) show the Raman confocal map using 785 nm excitation for SD1, SD4, and SD6 samples, respectively, which depicts spatial fluctuations in Raman shift across the sample. Sample SD1 shows the Raman shift at 1330.68 cm^{-1} for most of the region (shown in green), and some of the regions show the Raman shift at 1331.34 cm^{-1} (yellow patches), while other regions show around 1330 cm^{-1} (cyan). Sample SD4 shows a stable peak position at 1330.68 cm^{-1} throughout the sample, while varying Raman shifts are observed across the SD6 sample. The presence of non-diamond carbon, excitation wavelengths, and crystallite size influences the intensity and position of the diamond Raman line.[25] The variations in the crystallite size lead to a change in the lattice vibrations and, thus, result in a change in the Raman spectrum. It originates from phonon confinement that arises from smaller nanodiamonds or small scattering domains formed by diamond defects.[26,27] The SD4 and SD5 diamonds showcase a prominent diamond Raman line with reduced non-diamond carbon content and enhanced long-range lattice crystallinity, supported by a uniform distribution of Raman shift across the diamond surface. These combined features make SD4 and SD5 diamond samples superior to others in the present work. Concurrently, confocal Raman mapping has revealed spatial differences influenced by crystallite size and the presence of non-diamond carbon. Further, spectral and temporal PL mapping is used to validate defects present in the sample, as discussed below.

The PL study on diamond samples provides information regarding the nature of defects present in the sample. We have used a 532 nm excitation to excite both charge states of NVs in diamond. During relaxation, the transitions can be either spin-conserving, leading to PL spectra comprising ZPL and PSBs or spin-flip transitions, resulting in non-radiative transitions. Figure 2 shows the PL spectra of SD1 and SD4 samples, while the PL spectra of other samples are presented in Fig. S3 in the supplementary material. Figure 2(a) shows PL spectra measured from the SD1 sample (symbols), similar to PL spectra from SD2 and SD3 samples. The spatial-dependent PL spectra are acquired by scanning the sample, and it is observed that the spectral features do not change across the sample, albeit with a slight variation in PL intensity (Fig. S4 in the supplementary material). We observe distinct and sharp transitions in PL spectra at 574.62 ± 0.04 and 637.15 ± 0.04 nm, which correspond to ZPL transitions associated with NV^0 and NV^- charge states. Subsequently, a gradual ascent in PSB emission resulting from the involvement of phonons in the electronic transition process is observed up to 680 nm.

Figure 2(b) shows the emission spectra from the SD4 sample, which shows an intense peak at 575.72 ± 0.03 nm, corresponding to NV^0 ZPL, followed by PSB emission. The PSB emission shows an upward trend up to 637 nm and thereafter followed by a subsequent intensity reduction extending up to 850 nm. Importantly, no distinctive strong ZPL or PSB characteristics corresponding to NV^- are detected, unlike in the SD1 sample. A line scan across the sample shows similar spectral features (Fig. S4 in the supplementary material). The confocal PL scan across the sample allows for visualizing NV concentration on the sample surface (Fig. S7 in the supplementary material). Again, for all three samples SD4, SD5, and SD6, we do not observe NV^- ZPL. The sample SD6 shows similar spectral features with an additional peak around 742.65 ± 0.07 nm in PL spectra due to single-vacancy (V^0) defects in the diamond sample.[28–30] It is interesting to note that in

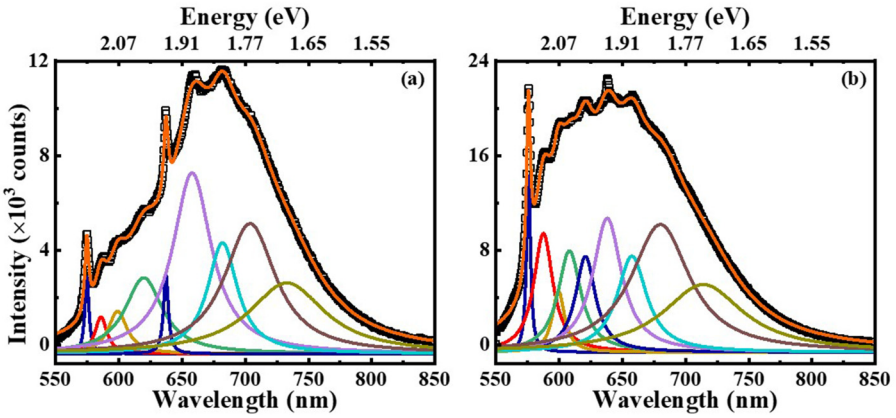

FIG. 2. The PL spectra of (a) SD1 and (b) SD4 samples. The PL spectra are deconvoluted to identify the ZPL and PSB transitions. The black squares show the experimental data and the solid orange line fits the data. The sharp transitions at 575 and 637 nm correspond to ZPLs of NV^0 and NV^- (shown in blue). For the SD1 sample, the sharp ZPL peak of NV^- is followed by the PSB of NV^-, which signifies the presence of NV^- charge state. However, the SD4 sample shows only one sharp peak at 575 nm with broad PSB transitions, which signifies the absence of an NV^- charge state.

Raman confocal mapping of SD1 and SD6 samples (Fig. 1), we observe the spatial variation in Raman shift, which corroborates with the intensity fluctuations in the PL contour map of these samples (Fig. S4 in the supplementary material). In contrast, the spatial uniformity of the Raman shift in SD4 is consistent with its uniform PL contour map. The spatial variation and presence of non-diamond carbon observed in Raman spectra arise from localized graphitization during the diamond growth process. These regions can introduce the non-radiative combination centers, leading to partial quenching of NV emission.

The SD7 sample, on the other hand, exhibits substantial spectral variations and significant intensity changes at distinct locations, as seen in the PL line scan (Fig. S4 in the supplementary material). Following their diverse spectral characteristics, we classify the PL spectra originating from SD7 sample into two distinct categories: SD7a and SD7b (Fig. S5 in the supplementary material). The SD7a showcases spectral attributes resembling those of SD1, while the SD7b displays spectra close to those observed for SD4 sample. However, under 473 nm excitation, all samples exhibit spectrally identical PL emissions that closely resemble the emissions from SD4 sample excited with 532 nm (Fig. S6 in the supplementary material). Upon excitation with 473 nm, only NV^0 charge state is excited, which is present in all samples. However, both NV charge states contribute to the emission for 532 nm excitation, Fig. S6(b) in the supplementary material shows the relative contribution of NV^- in emission spectra, normalized to ZPL of NV^0, from different samples.

To understand the reason behind distinct PL spectra, we estimate the charge state ratio by integrating the area under background-subtracted ZPL peaks in PL spectra, considering PSB transitions as background. The background corrected ZPLs are shown in Fig. S9(a) in the supplementary material. We define the charge state ratio as[31]

$$\text{Charge state ratio} = \frac{\text{ZPL area } (NV^-)}{\text{ZPL area } (NV^0 + NV^-)}. \quad (1)$$

The charge state ratio, calculated using PL spectra, for SD1 sample is 0.44 ± 0.01, indicating that about 44% (nearly half) of NVs are in the negative charge state, the highest of all samples in the present work. The calculated charge state ratio for SD4 sample is only 0.06 ± 0.01, which implies that emission originates predominantly from the NV^0 charge state. We also observe that the charge state ratio for NVs exhibits a negligible dependency on excitation laser power [Fig. S9(b) in the supplementary material]. This consistency is expected as the emission intensity from samples shows a linear dependence on excitation pump power (Fig. S8 in the supplementary material and Table S2 in the supplementary material). Thus, these results suggest that, under standard conditions, charge states of NV centers establish an equilibrium. Moreover, the mechanisms of photoionization and recombination of NV centers have negligible influence on altering this equilibrium for different excitation powers.

We have estimated the areal density of NVs using the confocal fluorescence map of samples in comparison with that of a single NV center from a high-quality diamond sample [Qnami AG; Fig. S6(c) in the supplementary material]. The NV density is estimated using the formula $n_{NV} = \frac{1}{C \cdot A} \sum C_i$, where $\sum C_i$ is the integrated count rate from the measured confocal map, A is the area of confocal map, and C is the average count rate for single NV. The estimated NV density for different samples used in the present work is given in Table I. As the average NV density decreases, the relative fluctuations in NV density increase. When the NV density is higher, fluctuations are reduced, which arises from uniform

TABLE I. Comparison of estimated NV density to the charge state ratio of NV centers among different samples considered in the present work.

Sample	SD1	SD2	SD3	SD4	SD5	SD6
Charge state ratio	0.44 ± 0.01	0.28 ± .07	0.32 ± 0.05	0.06 ± 0.01	0.14 ± 0.04	0.03 ± 0.03
NV density (NVs/μm^2)	29.44 ± 2.29	12.22 ± 1.32	19.52 ± 2.30	11.55 ± 6.78	11.07 ± 6.46	7.47 ± 5.69

availability of nitrogen at high concentrations, facilitating consistent NV formation. In contrast, limited nitrogen availability leads to inhomogeneous NV incorporation, resulting in greater spatial fluctuations. In sample SD6, there is a reduced efficiency of NV creation; as a result, a large fraction of vacancies remains unconverted and isolated in the sample. Sample SD7 exhibits even lower NV density, and thus, in order to effectively pump the system to the excited state, we have to use higher excitation power.

To quantify the absence of NV^- charge state, which was inferred using PL spectra, we measure the ODMR spectra for the corresponding samples. We employed a 660 ± 10 nm bandpass to filter out PL emission coinciding with both NV^0 and NV^- emission window. Figures 3(a) and 3(b) show the ODMR spectra corresponding to SD1 and SD4 samples. The measured ODMR spectra are fitted using the function, which is the solution to the Hamiltonian of the system,[32]

$$I(\omega) = 1 - \frac{\delta_{fi}\Delta\vartheta}{\left(4(\omega-\omega_0)^2 + (\Delta\vartheta)^2\right)^2}, \tag{2}$$

where δ_{fi} is the inter-system crossing (ISC) coupling coefficient, $\Delta\vartheta$ is the FWHM of the ODMR dip, and $\omega_0 = 2.87$ GHz corresponds to zero field splitting (ZFS) of the ground state of the NV^-. For the SD1 sample, we have obtained the dip in PL spectra at 2.88 ± 0.01 GHz, corresponding to the ZFS of the NV^- ground state (Fig. S2 in the supplementary material). The full-width at half-maxima (FWHM) of the ODMR dip is estimated to be 10.00 ± 0.36 MHz. We do not observe any strain-generated twofold splitting of the dip in the ODMR spectra, which indicates that these are strain-free diamond samples. The ODMR signal contrast (C) is estimated using the formula

$$C = \left(1 - \frac{I_{mw(on)su}}{I_{mw(off)}}\right) \times 100, \tag{3}$$

where $I_{mw(on)}$ and $I_{mw(off)}$ are the PL intensity at on- and off-resonance microwave frequency and the C value is a measure for assessing the quality of optical readout in ODMR measurements.[33] Hence, a high contrast is anticipated for accurately mapping NV^- spin states in diamonds. The estimated C value for SD1 sample is $1.14 \pm 0.12\%$ at an emission wavelength of 660 nm, which increases to $1.46 \pm 0.21\%$ at an emission wavelength of 700 nm. This increase in C value is potentially linked to reduced contribution from NV^0 charge state. However, the SD4 sample does not show any dip in the ODMR spectra, which shows the complete absence of NV^- charge state. This further supports our charge state estimation using PL spectra analysis with SD4 sample shows the minimum value of NV^- contribution. Figure 3(c) shows the measured ODMR spectra for SD7a, and the inset shows the ODMR for SD7b. A dip in PL counts at 2.88 GHz is evident with a C value of $1.27 \pm 0.26\%$ for SD7a, which is the signature of NV^-. The estimated FWHM is about 15.36 ± 3.61 MHz, slightly higher than SD1 sample. Surprisingly, at 700 ± 10 nm of emission wavelength, the SD7 sample shows a C value of about 2%, similar to reported values in the literature.[34,35] In the SD7 sample, the C value depends on the spatial location of excitation spot over the sample, and we have observed the absence of ODMR dip from specific locations on the sample. Notably, locations on SD7 showing the PL spectra with a strong 637 nm peak and its accompanying PSB akin to SD1 consistently exhibit a dip in the ODMR spectra. The locations showing PL spectra of SD7b consistently lack ODMR dip similar to SD4 samples. Thus, the measured PL and ODMR spectra are correlated with the presence of NV^- charge state in samples. Since the NV is an active system, and therefore, we have measured continuous ODMR spectra. The ODMR spectrum also supports the high NV^-/NV^0 charge state ratio. The ODMR measurements are used to confirm the analysis by the PL spectra on the quantification of NV^- presence in the sample. However, higher ODMR contrast can be achieved using pulsed microwave schemes combined with optimized spin initialization and readout protocols, which we plan to explore in future work.

The measured PL spectra are deconvoluted into various Lorentzian peaks to deduce ZPL and PSB transition energies. The Lorentzian function is used to fit the measured PL spectra,[36]

$$I(E) = \frac{2A}{\pi}\left(\frac{\Delta E}{4(E-Ec)^2 + \Delta E^2}\right), \tag{4}$$

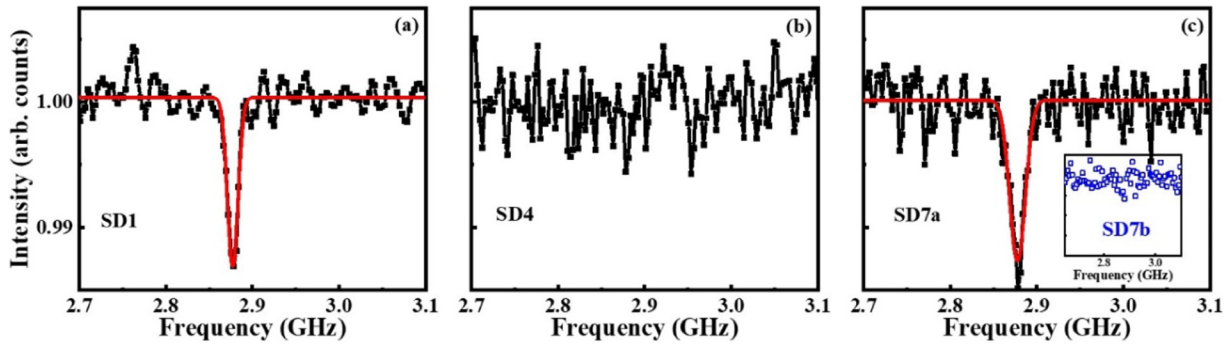

FIG. 3. The ODMR spectra of (a) SD1, (b) SD4, and (c) SD7 samples. SD1 showed the dip at 2.88 GHz with a contrast of $1.14 \pm 0.12\%$. SD4 does not show any dip in the spectra due to the absence of spin-dependent non-radiative transitions and, hence, absence of NV^-. A PL dip at 2.88 GHz is observed only at locations displaying the SD7a type PL, whereas locations displaying SD7b type PL show no ODMR dip (shown in the inset).

where E_c is the emission peak center, ΔE is the FWHM, and A is the area under the peak. We have used an iterative nonlinear least square fitting method to optimize fitting parameters. The iterations continue until the chi-square value (χ^2) difference falls below 5% for consecutive iterations. The optical transitions are fitted using nine Lorentzian curves for samples SD1 and SD4 as shown in Figs. 2(a) and 2(b), respectively. The maximum displacement of the PSBs from their ZPLs is 165 meV in diamonds.[30,37] For the SD1 sample, NV^0 exhibits prominent PSBs at 585.73 ± 0.06, 598.84 ± 0.16, and 619.53 ± 0.12 nm. Their respective energy shifts from NV^0 ZPL line are 40.93 ± 0.30, 87.30 ± 0.60, and 156.44 ± 0.43 meV. Similarly, the NV^- charge state exhibits PSBs at 657.93 ± 0.05, 681.97 ± 0.04, and the corresponding energy shifts from ZPL line of NV^- is 61.47 ± 0.18 and 127.90 ± 0.53 meV, respectively (Table S1 in the supplementary material). For the SD4 sample, the PSBs of NV^0 are at 587.43 ± 0.07, 599.45 ± 0.10, 607.99 ± 0.40, and 620.81 ± 0.06 nm. The respective shift in energy from the NV^0 ZPL is 42.95 ± 0.26, 85.27 ± 0.37, 114.31 ± 1.35, and 156.44 ± 0.22 meV. In our analysis, the number of peaks used to fit the NV^- and NV^0 phonon sidebands is chosen based on the spectral complexity observed in each sample and the need to capture the sub-structure features arising from phonon-assisted transitions. Specifically, for SD4, SD5, and SD6 samples, more fitting components were required for NV^0 compared to SD1–SD3 samples due to richer spectral structure and broader PSB features. The electron–phonon coupling would also vary depending on nitrogen concentration, and hence the formation of the NV charge state ratio among the samples. Our results also confirm that the PSB emission from NV center does not show a simple multiplicative relationship of energy shifts from ZPLs, in contrast to earlier reports.[30] This uneven energy shift arises from the anharmonic nature of energy states, which increases with an increase in the charge state ratio (Fig. S10 in the supplementary material and Table S1 in the supplementary material). The increased electron–electron repulsion is responsible for an increase in the observed anharmonicity. The presence of non-bonding valance electrons leads to a nonlinear repulsive force with neighboring bonds, leading to anharmonicity.[38] The nonlinear repulsive forces increase when the NV^0 traps an extra electron to form NV^- charge state, thus leading to an increased anharmonicity depending on the charge state ratio. Carbon atomic wires also show such anharmonic nature in vibrational levels.[39] We have observed the variation in NV^- ZPL position from 636.56 ± 0.63 to 638.45 ± 0.18 nm whereas the ZPL of single NV center in high-quality diamond crystal appears at 637.5 nm [Fig. S6(c) in the supplementary material]. The local environment of NV centers in diamonds varies depending on the nitrogen content, resulting in the emission properties. Specifically, an increased concentration of impurities surrounding NV centers increases their susceptibility to surrounding environment, ultimately resulting in structural deformations and stress induction within NV centers. Therefore, we can consider that the change in nitrogen concentration and charge state ratio decides the variation in ZPL wavelength, phonon energy, and Debye–Waller (DW) factor.

The PSBs show broadened transitions compared to narrow ZPL transitions. The broadening of these transitions is mainly due to (i) spontaneous emission, (ii) pure dephasing, and (iii) phonon emissions.[36] The phonon-induced broadening is much more pronounced than the pure dephasing, which is also evident from PL spectra fit. The fitting of PL spectra yields an FWHM value of 71.26 ± 14.33 meV for the transition at 637 nm for the SD4 sample. However, for the ZPL transition at 575 nm, which is consistent for both SD1 and SD4 samples, as well as the ZPL transition at 637 nm for SD1 sample, the FWHM remains notably narrower, which is about 15 meV only. To assess the relative broadening of these transitions, we define monochromaticity (M), $M = \Delta E/E_c$, where ΔE is the FWHM and E_c is the transition energy, which dictates the degree of coherence of a transition in the diamond. The value of M for the PSB transitions is ten times higher than the ZPL transition, as expected for non-coherent PSB transitions. The M value for both ZPL transitions in SD1 is $0.01 \pm 1 \times 10^{-4}$, while that for PSB transition is $0.06 \pm 1 \times 10^{-4}$ at 657.93 ± 0.05 nm, which is about six times that of ZPL. However, the M value is $0.01 \pm 1 \times 10^{-3}$ and $0.04 \pm 1 \times 10^{-3}$ for 575 and 637 nm, respectively, for the SD4 sample. Thus, substantial broadening observed at 637 nm peak for the SD4 sample [blue line in Fig. 2(b)] is due to phonon-induced transitions, compared with the broadening of the same band in SD1, which further corroborates the absence of NV^-. The subsequent ODMR measurements and transition broadening at 637 nm for the SD4 sample conclusively establish a lower charge state ratio of NV and reinforce that the effective emission arises majorly from the NV^0 charge state. Table S2 in the supplementary material summarizes the estimated charge state ratio for all samples and center wavelengths corresponding to various transitions and their energies, M, and DW factor.

The fast decay rate and strong ZPL emission are the essential requirements for NVs. The DW factor signifies the fraction of total emission channeled into ZPL.[40] The DW factor associated with each charge state is defined as

$$\mathrm{DW} = \frac{\int d\lambda I_{ZPL}}{\int d\lambda I_{ZPL} + \int d\lambda\, I_{PSBs}}, \tag{5}$$

where $\int d\lambda I_{ZPL}$ represents the effective integrated intensity of ZPL and $\int d\lambda\, I_{PSBs}$ corresponds to the integrated intensity of PSBs for respective charge state. To prevent spectral overlap from artificially affecting the DW factor, the effective ZPL intensity is determined after background correction, treating PSB contributions as a background [Fig. S9(a) in the supplementary material]. In contrast, the PSB contributions are extracted from fitted Lorentzian components. This method ensures that the overlapping emission spectra of NV^0 and NV^- do not artificially influence the DW factor, particularly when the charge state ratio changes. The estimated DW factor for SD1 is $3.04 \pm 0.07\%$ and $0.45 \pm 0.02\%$ for NV^0 and NV^- charge states, respectively. For SD4, it is $4.11 \pm 0.23\%$ and $0.25 \pm 0.04\%$ for NV^0 and NV^-, respectively. It implies that the intensities of transitions involving phonon emission are stronger than pure electronic transitions in both charge states. Also, the probability of pure electronic transitions is higher for NV^0 than for NV^-. The DW factor as a function of charge state ratio corresponding to different samples is given in Fig. 4. The NV^- DW factor increases by 3.5 times, while it decreases by 1.7 times for NV^0. The increase in the NV charge state ratio increases the fraction of photons that are emitted into ZPL. The fraction of photons emitting via pure

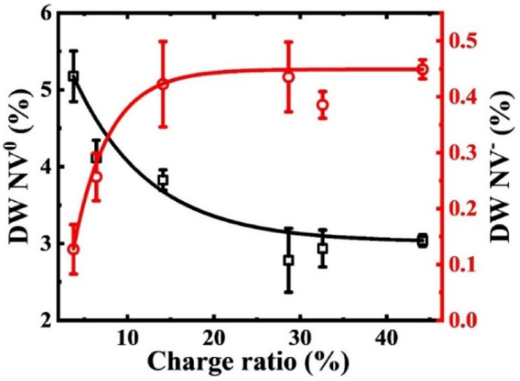

FIG. 4. The DW factor of NV^0 and NV^- as a function of charge ratio corresponding to different samples. The DW factor improves for NV^- with an increase in charge state ratio (track lines are guide to eyes). The increase in DW factor is saturated over a charge state ratio of ∼15% because PSB intensity also increases with an increase in the charge state ratio.

electronic transition for NV^0 charge state decreases with an increase in the charge state ratio of NV. The plot confirms the increased NV^- DW factor for samples with a higher charge state ratio.

To understand the charge state-dependent emission dynamics of NV center, we have measured the NV center excited state lifetime across the emission spectrum as a function of charge state ratio. Figure 5 shows the excited state lifetime of NV center as a function of charge state ratio corresponding to samples at various emission wavelengths. For SD1 sample (44% charge state ratio), we observe a decrease in lifetime with an increase in the emission

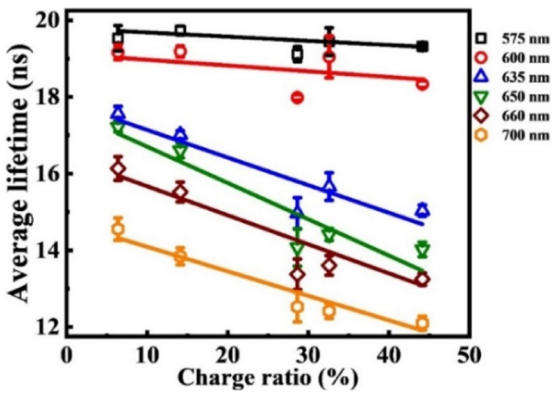

FIG. 5. The average lifetime of excited state of NV at various emission wavelengths as a function of charge state ratio corresponding to different samples. At each charge state ratio, the lifetime decreases with increased emission wavelength. At 575 nm (ZPL of NV^0) and 600 nm (PSB of NV^0), the lifetime remains constant irrespective of the charge state ratio. In the NV^- emission region, the lifetime value decreases with an increased charge state ratio (track lines are guide to eyes).

wavelength. The average lifetimes at the ZPLs of NV^0 and NV^- are 19.32 ± 0.04 and 15.03 ± 0.15 ns, respectively, which further reduce to 12.10 ± 0.18 ns at an emission wavelength of 700 nm. The uncertainty $\delta\tau$, of average lifetime $<\tau>$, is the standard deviation of several trials at different locations on the sample for the corresponding spectral emission window. The average lifetime for the SD1 sample shows an overall reduction with increased emission wavelength. We have observed a 22% decrease in average lifetime as the emission wavelength changes from ZPL of NV^0 to ZPL of NV^-. The average lifetime further reduces by 37% at 700 nm of emission wavelength. Furthermore, from the trend in lifetimes of SD4 sample, solitary from NV^0 (∼5% charge ratio), we can deduce that the emission decay rate inherently increases for longer emission wavelengths. This observation is also consistent for each charge state ratio. However, SD6 samples, despite the lower charge ratio, exhibit a reduced lifetime across the emission spectra (Fig. S11 in the supplementary material). This deviation is attributed to the local environment, specifically the presence of V^0 exclusively in SD6. Therefore, we deduce that the decrease in lifetime with increasing emission wavelength is a general characteristic of NV emission decay, consistent across all charge ratios.

Within the NV^0 emission window (at 575 and 600 nm), the lifetime remains independent of the charge state ratio, whereas at higher wavelengths, it decreases with an increase in the charge state ratio. This spectral-dependent decay rate confirms NV^- dominance at longer wavelengths and NV^0 dominance at shorter wavelengths. The lifetime of NV^0 charge state is ∼19 ns and NV^- exhibits a more complex decay profile. A simplified electronic energy level diagram for NV^- is shown in Fig. S2 in the supplementary material. The $m_s = 0$ spin sublevel of the excited triplet state relaxes directly to the $m_s = 0$ spin sublevel of the ground state. In contrast, system from $m_s = \pm 1$ spin sublevel has a finite probability of undergoing non-radiative relaxation via intersystem crossing (ISC) along with radiative spin-conserving transitions directly to $m_s = \pm 1$ spin sublevel of the ground state. The decay rate of population from ith level is given by the rate equation

$$\frac{dn_i}{dt} = \sum_j (k_{ji} n_i - k_{ij} n_i), \tag{6}$$

where n_i is the population of ith level, and k_{ij} is the rate of transition from ith level to jth level. Hence, the excited sublevel $m_s = \pm 1$ decays faster than $m_s = 0$ sublevel. The reported lifetime value for the $m_s = 0$ spin state is ∼13 ns, whereas that for the $m_s = \pm 1$ spin state is ∼8 ns.[41] At the same time, improper spin polarization of the NV^- charge state results in a bi-exponential decay curve.[42,43] For example, when the system is directly excited with a picosecond pulse, it results in improper spin polarization, and the emission comes from both spin states. The difference in the measured lifetime between the two charge states is due to spin-dependent non-radiative transition to the metastable state rather than a change in transition oscillator strength.

Therefore, the lifetime difference between the two charge states arises from the complex energy level structure of NV^- and the associated non-radiative relaxation processes. As the emission

shifts from a shorter to longer wavelength, the contribution from the NV^- charge state dominates, as well as the coupling to metastable state also increases. Thus, a collective decrease in lifetime is observed with increased emission wavelengths at higher charge ratios of NV. Our results are helpful for solely PL-based interpretation of charge state ratios with high spatial resolution, which is important to develop a NV based magnetometer, where determining and achieving a high charge state ratio of NV^- is pivotal. These results further suggest that longer wavelength photons emitted from a high NV^- charge state ratio are suitable for single photon applications where on-demand triggered photons are required.

IV. CONCLUSIONS

We have studied the charge state ratio induced changes in the spectral and temporal properties of NV centers in CVD grown diamonds. The broad features around 1170–1450 cm^{-1} in the Raman spectra are observed effectively under 785 nm which are otherwise absent for 473 and 532 nm excitations. Narrow 637 nm transitions in the SD1 sample correspond to the ZPL, confirming the NV^- presence, supported by ODMR measurements. In contrast, broadened transitions at 637 nm in the SD4 sample suggest the absence of NV^-, corroborated by the absence of ODMR dip. A sample with a higher charge state ratio showed the higher anharmonicity of vibrational levels. Furthermore, the DW factor of NV^- increases by 3.53 times, while that of NV^0 decreases by 1.7 times with an increase in the charge state ratio. We have observed a maximum decrease of about 37% in average lifetime, resulting from the combined contribution of an increased charge state ratio and changes in emission wavelength from 575 to 700 nm. Understanding the wavelength-dependent lifetime of NVs in diamonds is crucial for super-resolution techniques like stimulated emission depletion, where the ability to suppress fluorescence is pivotal. The use of PL based charge state ratio estimation supported by ODMR measurements helps in the design of diamond samples for quantum sensing like a NV based magnetometer.

SUPPLEMENTARY MATERIAL

See the supplementary material for detailed Raman spectra of different diamond samples, energy level diagram of NV centers, detailed PL spectra of various samples, confocal images, charge state ratio calculations, and spectral-dependent decay rate measurements.

ACKNOWLEDGMENTS

The authors acknowledge financial support from IIT Ropar, DST-ICPS (No. DST/ICPS/QuST/Theme-2019/General), DST-SERB (No. SB/SJF/2020-21/05), and Swarnajayanti Fellowship (No. DST/SJF/PSA-01/2019-20). R.V.N. acknowledges Chanakya fellowship support from I-HUB Quantum Technology Foundation, IISER Pune. A.R. thanks the support from PMRF for Ph.D. program and R.D. thanks CSIR-UGC fellowship for Ph.D.

AUTHOR DECLARATIONS

Conflict of Interest

The authors have no conflicts to disclose.

Author Contributions

Ashish Redhu: Conceptualization (supporting); Formal analysis (lead); Investigation (lead); Writing – original draft (lead); Writing – review & editing (equal). **Rahul Dhankhar:** Formal analysis (supporting); Investigation (supporting); Writing – original draft (supporting). **Sushmita Dey:** Investigation (supporting); Methodology (supporting); Resources (supporting); Writing – review & editing (supporting). **Rajesh V. Nair:** Conceptualization (lead); Formal analysis (equal); Project administration (lead); Supervision (lead); Writing – review & editing (equal).

DATA AVAILABILITY

The data that support the findings of this study are available within the article and its supplementary material.

REFERENCES

[1]G. Balasubramanian, P. Neumann, D. Twitchen, M. Markham, R. Kolesov, N. Mizuochi, J. Isoya, J. Achard, J. Beck, J. Tissler, V. Jacques, P. R. Hemmer, F. Jelezko, and J. Wrachtrup, "Ultralong spin coherence time in isotopically engineered diamond," Nat. Mater. **8**(5), 383–387 (2009).
[2]S. Li, J.-P. Chou, J. Wei, M. Sun, A. Hu, and A. Gali, "Oxygenated (113) diamond surface for nitrogen-vacancy quantum sensors with preferential alignment and long coherence time from first principles," Carbon **145**, 273–280 (2019).
[3]T. Tsuji, T. Sekiguchi, T. Iwasaki, and M. Hatano, "Extending spin dephasing time of perfectly aligned nitrogen-vacancy centers by mitigating stress distribution on highly misoriented chemical-vapor-deposition diamond," Adv. Quantum Technol. **7**(1), 2300194 (2024).
[4]S. Kumar, M. Nehra, D. Kedia, N. Dilbaghi, K. Tankeshwar, and K.-H. Kim, "Nanodiamonds: Emerging face of future nanotechnology," Carbon **143**, 678–699 (2019).
[5]F. Jelezko, T. Gaebel, I. Popa, A. Gruber, and J. Wrachtrup, "Observation of coherent oscillations in a single electron spin," Phys. Rev. Lett. **92**(7), 076401 (2004).
[6]P.-B. Li, Z.-L. Xiang, P. Rabl, and F. Nori, "Hybrid quantum device with nitrogen-vacancy centers in diamond coupled to carbon nanotubes," Phys. Rev. Lett. **117**(1), 015502 (2016).
[7]J. R. Maze, P. L. Stanwix, J. S. Hodges, S. Hong, J. M. Taylor, P. Cappellaro, L. Jiang, M. V. G. Dutt, E. Togan, A. S. Zibrov, A. Yacoby, R. L. Walsworth, and M. D. Lukin, "Nanoscale magnetic sensing with an individual electronic spin in diamond," Nature **455**(7213), 644–647 (2008).
[8]M. Fazeli Jadidi, H. Ö. Özer, S. Goel, J. I. Kilpatrick, N. McEvoy, D. McCloskey, J. F. Donegan, and G. L. W. Cross, "Distribution of shallow NV centers in diamond revealed by photoluminescence spectroscopy and nanomachining," Carbon **167**, 114–121 (2020).
[9]E. Bourgeois, J. Soucek, J. Hruby, M. Gulka, and M. Nesladek, "Photoelectric detection of nitrogen-vacancy centers magnetic resonances in diamond: Role of charge exchanges with other optoelectrically active defects," Adv. Quantum Technol. **5**(5), 2100153 (2022).
[10]S. Sharma and R. V. Nair, "Nanophotonic control of the color center emission from nanodiamonds," Opt. Lett. **43**(16), 3989–3992 (2018).
[11]Y. Mita, "Change of absorption spectra in type-Ib diamond with heavy neutron irradiation," Phys. Rev. B **53**(17), 11360–11364 (1996).

[12]P. Siyushev, H. Pinto, M. Vörös, A. Gali, F. Jelezko, and J. Wrachtrup, "Optically controlled switching of the charge state of a single nitrogen-vacancy center in diamond at cryogenic temperatures," Phys. Rev. Lett. **110**(16), 167402 (2013).
[13]C. Bradac, T. Gaebel, N. Naidoo, M. J. Sellars, J. Twamley, L. J. Brown, A. S. Barnard, T. Plakhotnik, A. V. Zvyagin, and J. R. Rabeau, "Observation and control of blinking nitrogen-vacancy centres in discrete nanodiamonds," Nat. Nanotechnol. **5**(5), 345–349 (2010).
[14]H. Kawashima, H. Kato, M. Ogura, D. Takeuchi, T. Makino, and S. Yamasaki, "Desorption time of phosphorus during MPCVD growth of n-type (001) diamond," Diamond Relat. Mater. **64**, 208–212 (2016).
[15]K.-M. C. Fu, C. Santori, P. E. Barclay, and R. G. Beausoleil, "Conversion of neutral nitrogen-vacancy centers to negatively charged nitrogen-vacancy centers through selective oxidation," Appl. Phys. Lett. **96**(12), 121907 (2010).
[16]S. A. Savinov, V. V. Sychev, and D. Bi, "Diamond nitrogen-vacancy center charge state ratio determination at a given sample point," J. Lumin. **248**, 118981 (2022).
[17]M. Jani, M. Mrózek, A. M. Nowakowska, P. Leszczenko, W. Gawlik, and A. M. Wojciechowski, "Role of high nitrogen-vacancy concentration on the photoluminescence and Raman spectra of diamond," Phys. Status Solidi A **220**(4), 2200299 (2023).
[18]P. V. Zinin, I. Kudryashov, N. Konishi, L. C. Ming, V. L. Solozhenko, and S. K. Sharma, "Identification of the diamond-like B–C phase by confocal Raman spectroscopy," Spectrochim. Acta, Part A **61**(10), 2386–2389 (2005).
[19]J. Filik, J. N. Harvey, N. L. Allan, P. W. May, J. E. P. Dahl, S. Liu, and R. M. K. Carlson, "Raman spectroscopy of nanocrystalline diamond: An *ab initio* approach," Phys. Rev. B **74**(3), 035423 (2006).
[20]N. N. Ovsyuk, S. V. Goryainov, and A. Y. Likhacheva, "Raman scattering of impact diamonds," Diamond Relat. Mater. **91**, 207–212 (2019).
[21]M. Ayiania, E. Weiss-Hortala, M. Smith, J.-S. McEwen, and M. Garcia-Perez, "Microstructural analysis of nitrogen-doped char by Raman spectroscopy: Raman shift analysis from first principles," Carbon **167**, 559–574 (2020).
[22]C. Xiao, F. Elam, S. van Vliet, R. Bliem, S. Lépinay, N. Shahidzadeh, B. Weber, and S. Franklin, "Intercrystallite boundaries dominate the electrochemical corrosion behavior of polycrystalline diamond," Carbon **200**, 1–9 (2022).
[23]J. Wagner, C. Wild, and P. Koidl, "Resonance effects in Raman scattering from polycrystalline diamond films," Appl. Phys. Lett. **59**(7), 779–781 (1991).
[24]A. C. Ferrari, J. Robertson, A. C. Ferrari, and J. Robertson, "Raman spectroscopy of amorphous, nanostructured, diamond–like carbon, and nanodiamond," Philos. Trans. R. Soc., A **362**(1824), 2477–2512 (2004).
[25]V. N. Mochalin, O. Shenderova, D. Ho, and Y. Gogotsi, "The properties and applications of nanodiamonds," Nat. Nanotechnol. **7**(1), 11–23 (2012).
[26]I. H. Campbell and P. M. Fauchet, "The effects of microcrystal size and shape on the one phonon Raman spectra of crystalline semiconductors," Solid State Commun. **58**(10), 739–741 (1986).
[27]S. Osswald, V. N. Mochalin, M. Havel, G. Yushin, and Y. Gogotsi, "Phonon confinement effects in the Raman spectrum of nanodiamond," Phys. Rev. B **80**(7), 075419 (2009).
[28]K. Ganesan, P. K. Ajikumar, S. Ilango, G. Mangamma, and S. Dhara, "Si and N-vacancy color centers in discrete diamond nanoparticles: Raman and fluorescence spectroscopic studies," Diamond Relat. Mater. **92**, 150–158 (2019).
[29]C. Yang, Z. Mi, H. Jin, T. Venkatesan, R. Vispute, and A. A. Bettiol, "Large-scale fabrication of surface SiV− centers in a flexible diamond membrane," Carbon **203**, 842–846 (2023).
[30]R. Guo, K. Wang, Y. Tian, and H. Wang, "Nitrogen vacancy luminescence and their phonon sidebands characteristics in nitrogen-doped diamond," J. Alloys Compd. **924**, 166507 (2022).
[31]D. B. Radishev, M. A. Lobaev, S. A. Bogdanov, A. M. Gorbachev, A. L. Vikharev, and M. N. Drozdov, "Investigation of NV centers charge states in CVD diamond layers doped by nitrogen and phosphorous," J. Lumin. **239**, 118404 (2021).
[32]Y. Rosenzweig, Y. Schlussel, and R. Folman, "Probing the origins of inhomogeneous broadening in nitrogen-vacancy centers with Doppler-free-type spectroscopy," Phys. Rev. B **98**(1), 014112 (2018).
[33]L. Rondin, J. P. Tetienne, T. Hingant, J. F. Roch, P. Maletinsky, and V. Jacques, "Magnetometry with nitrogen-vacancy defects in diamond," Rep. Prog. Phys. **77**(5), 056503 (2014).
[34]B. W. Blankenship, Z. Jones, N. Zhao, H. Singh, A. Sarkar, R. Li, E. Suh, A. Chen, C. P. Grigoropoulos, and A. Ajoy, "Complex three-dimensional microscale structures for quantum sensing applications," Nano Lett. **23**(20), 9272 (2023).
[35]A. Kuwahata, T. Kitaizumi, K. Saichi, T. Sato, R. Igarashi, T. Ohshima, Y. Masuyama, T. Iwasaki, M. Hatano, F. Jelezko, M. Kusakabe, T. Yatsui, and M. Sekino, "Magnetometer with nitrogen-vacancy center in a bulk diamond for detecting magnetic nanoparticles in biomedical applications," Sci. Rep. **10**(1), 2483 (2020).
[36]R. Albrecht, A. Bommer, C. Deutsch, J. Reichel, and C. Becher, "Coupling of a single nitrogen-vacancy center in diamond to a fiber-based microcavity," Phys. Rev. Lett. **110**(24), 243602 (2013).
[37]K. Wang, J. W. Steeds, Z. Li, and Y. Tian, "Photoluminescence studies of both the neutral and negatively charged nitrogen-vacancy center in diamond," Microsc. Microanal. **22**(1), 108–112 (2016).
[38]E. J. Skoug and D. T. Morelli, "Role of lone-pair electrons in producing minimum thermal conductivity in nitrogen-group chalcogenide compounds," Phys. Rev. Lett. **107**(23), 235901 (2011).
[39]P. Marabotti, M. Tommasini, C. Castiglioni, S. Peggiani, P. Serafini, B. Rossi, A. Li Bassi, V. Russo, and C. S. Casari, "Synchrotron-based UV resonance Raman spectroscopy probes size confinement, termination effects, and anharmonicity of carbon atomic wires," Carbon **216**, 118503 (2024).
[40]H.-Q. Zhao, M. Fujiwara, and S. Takeuchi, "Suppression of fluorescence phonon sideband from nitrogen vacancy centers in diamond nanocrystals by substrate effect," Opt. Express **20**(14), 15628–15635 (2012).
[41]D. C. Jones, Y. Alexandrov, N. Curry, S. Kumar, P. M. P. Lanigan, C. D. McGuinness, M. W. Dale, D. J. Twitchen, D. Fisher, M. A. A. Neil, C. Dunsby, and P. M. W. French, "Multidimensional spectroscopy and imaging of defects in synthetic diamond: Excitation-emission-lifetime luminescence measurements with multiexponential fitting and phasor analysis," J. Phys. D: Appl. Phys. **54**(4), 045303 (2021).
[42]A. Batalov, C. Zierl, T. Gaebel, P. Neumann, I. Y. Chan, G. Balasubramanian, P. R. Hemmer, F. Jelezko, and J. Wrachtrup, "Temporal coherence of photons emitted by single nitrogen-vacancy defect centers in diamond using optical Rabi-oscillations," Phys. Rev. Lett. **100**(7), 077401 (2008).
[43]L. Robledo, H. Bernien, T. V. D. Sar, and R. Hanson, "Spin dynamics in the optical cycle of single nitrogen-vacancy centres in diamond," New J. Phys. **13**(2), 025013 (2011).